



# High-speed X-ray study of process dynamics caused by surface features during continuous-wave laser polishing

Patrick Faue<sup>a</sup>, Lewin Rathmann<sup>b</sup>, Marius Möller<sup>b</sup>, Mahmudul Hassan<sup>a</sup>, Samuel J. Clark<sup>c</sup>, Kamel Fezzaa<sup>c</sup>, Kevin Klingbeil<sup>d</sup>, Brodan Richter<sup>a</sup>, Joerg Volpp<sup>e</sup>, Tim Radel<sup>b</sup>, Frank E. Pfefferkorn (1)<sup>a,\*</sup>

<sup>a</sup> Department of Mechanical Engineering, University of Wisconsin-Madison, Madison, WI 53706 USA

<sup>b</sup> Bremer Institut für angewandte Strahltechnik GmbH, Bremen 28359, Germany

<sup>c</sup> X-ray Science Division, Advanced Photon Source, Argonne National Laboratory, Lemont, IL 60439, USA

<sup>d</sup> Cross Product Solutions, LLC, Osceola, WI 54020, USA

<sup>e</sup> Department of Engineering Sciences and Mathematics, Luleå University of Technology, Luleå, 971 87 Sweden

## ARTICLE INFO

### Article history:

Available online 17 April 2023

### Keywords:

Laser  
Polishing  
X-ray imaging

## ABSTRACT

During high-speed X-ray imaging of laser surface polishing experiments of specimens of 316L stainless steel at Argonne National Lab's Advanced Photon Source, it was discovered that the induced keyhole changes shape and dimensions while crossing an engineered surface feature without altering process parameters. It was observed that the post-surface feature keyhole was deeper than that of the pre surface feature keyhole. This work reports on the first in-situ observation of the effect of localized surface geometry on underlying melt pool behavior. This has implications for defect formation mechanisms during laser melting processes that rely on melt pool geometry.

© 2023 CIRP. Published by Elsevier Ltd. All rights reserved.

## 1. Introduction

Laser polishing is generally distinguished between continuous wave (cw) and pulsed (pw) polishing. The surface condition before laser polishing determines the polishing result as surface components with high amplitudes or spatial wavelengths larger than a threshold wavelength cannot be fully removed during polishing. In the cw-regime, it was shown that, in addition to the widely applied heat conduction regime, the keyhole regime offers advantages, especially for removing high initial roughness, as is typically the case on additively manufactured components [1]. High laser beam intensities applied on a material surface lead to the creation of a highly dynamic vapor channel which is referred to as a keyhole. Multiple attempts have been made to describe the complex phenomenon including experimental and modeling approaches. Typically, it has been assumed that one parameter set, e.g., a certain beam shape [2], leads to a defined keyhole shape. Even keyhole evolution simulations [3,4] show that there should be one solution for the resulting keyhole shape. A significant influence of the surface topography on the keyhole is generally not considered. In-situ high-speed X-ray imaging has been used to experimentally investigate the keyhole behavior. Thereby nominally flat surfaces were investigated in powder bed fusion [5] and laser remelting [1]: i.e., no surface texture other than that presented by loose or partially adhered powder particles. No published study has examined the influence of surface features on the melt pool shape and dynamics.

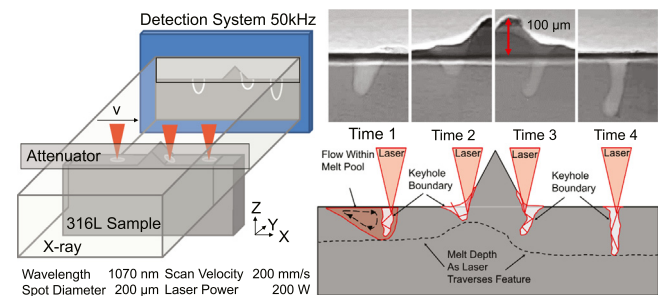


Fig. 1. The remelting process was observed using high-speed X-ray imaging (HSXRI).

In this study the authors use high-speed high-intensity X-ray imaging to capture the significant changes in the keyhole as it traverses across an engineered surface feature (Fig. 1). This new knowledge of the process will help understand the laser remelting dynamics of a laser beam-based, powder bed fusion of a metal substrate (PBF-LB/M) surface with roughness, waviness, and partially adhered particles.

## 2. Methods

### 2.1. Materials and surface preparation

Precision engineered surfaces were generated with a single surface feature on 316L stainless steel feedstock by milling a surface with a 9.525 mm (3/8 inch) diameter endmill with a feed per pass

\* Corresponding author.

E-mail address: [frank.pfefferkorn@wisc.edu](mailto:frank.pfefferkorn@wisc.edu) (F.E. Pfefferkorn).

equal to the endmill diameter. The resultant surface feature was a result of the endmill having a nose radius and not a sharp, right angle at its edge. The feedstock had been precision ground to 10 mm thickness before milling. Electronic discharge machining (EDM) was used to section the samples along the width of the bar stock into 10 mm tall, 0.6 mm thick samples with the single features extending upward from the top 10 mm × 0.6 mm surface. The surface features were approximately 100 μm tall and 200 μm at the base (Fig. 2). The sides of the samples were manually polished in incremental steps to 1 μm solution until the thickness of the samples were between 0.4 mm and 0.5 mm thick. The side surfaces are the surfaces through which the X-rays transmit, hence any roughness is variable average thickness across the sample that can result in noise in the images.

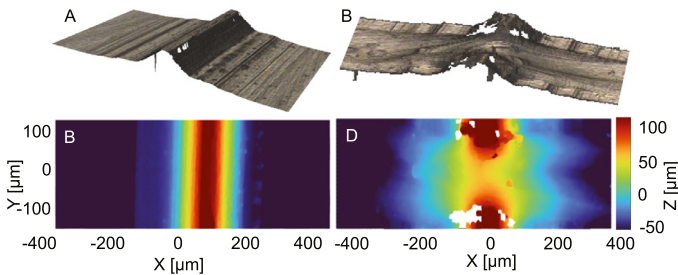


**Fig. 2.** Images of the surfaces: a single unpolished 100 μm tall feature (a, b) and (c, d) after laser polishing through remelting.

## 2.2. Laser polishing

Laser polishing of the samples was performed using an additive manufacturing set up (laser, scanhead, controls, and enclosure) whose purpose is to perform laser powder fusion experiments while high speed X-ray imaging at the Advanced Photon Source [5]. The laser used was a fiber laser emitting a Gaussian beam at 1070 nm in cw mode and was controlled by a SCANLAB IntelliScan 30-de scan head. The single features were polished using a 200 μm beam diameter achieved by operating defocused below the focal plane. The beam waist was measured at 42 μm with an effective  $M^2$  value of 1.091. The complete laser beam characterization is provided in the appendix. By defocusing the beam to 200 μm, the laser was incident to the sample well outside of the Rayleigh length and the spot size variation from the top to bottom of the surface feature was estimated to be under 10 μm based on the gaussian beam parameters from the beam characterization, thus minimizing local laser intensity variation due to variable surface height. The laser parameters were 200 W power and 200 mm/s scanning velocity. Imaging was performed on the last 2 mm of a 5 mm line scan to allow a reduction in the transient effects at the start of a line pass.

## 2.3. High speed X-ray imaging

High speed X-ray imaging was performed at Argonne National Lab's Advanced Photon Source using the 32-ID-B beamline. High-speed X-ray imaging was performed with a polychromatic X-ray beam with a first harmonic energy of ~24 keV and an energy bandwidth of ~7% generated by a 1.8 cm short period undulator with a gap of 11.5 mm. The samples that are oriented such that the top surface is centered in the image and a single feature is present within the window. The portion of X-ray beam that is transmitted through the sample is incident upon a 100 μm thick LuAG:Ce scintillator. The visible light is collected by a 10× optical system coupled with a high-speed camera (Photron, FASTCAM SA-Z 2100 K) to capture the visible light that is emitted by the scintillator. The high-speed imaging was performed at 50 kHz frame rate and used an exposure time of 19 μs per frame. The window imaged was 2 mm in width and 0.5 mm in height. The spatial resolution was 2 μm/pixel in both dimensions.

As an X-ray beam travels through a metallic sample, a large portion of it is attenuated by the sample. The X-rays that pass through the sample are incident to the scintillator to induce fluorescence with a brightness that is proportional to the local intensity of X-rays. This is known as an indirect X-ray detection system. The brightness of each pixel represents the relative attenuation by material along the path the X-ray travels through at the location of said pixel relative to the rest of the pixels in the image frame. Less material at the location of a pixel results in less X-ray absorption, more scintillator fluorescence, and a brighter pixel. This relationship between mean density relative and pixel brightness relative to the other pixels is known to follow the Beers–Lambert law.

In this work we imaged laser polishing with samples in an inert argon atmosphere. A thin titanium sheet was placed upstream in the X-ray path and is oriented such that it is in the frame of the image with its bottom edge barely overlapping with the top of the sample surface (Fig. 1). This acts to attenuate the raw X-ray beam in the region above the sample where there would otherwise be no metal to attenuate the beam before it strikes the scintillator. This attenuator allows high power X-ray beams to be used for thicker samples without saturating the pixels in the region above the sample or damaging the scintillator. Videos and individual image frames can be found in the Appendix.

## 2.4. Image processing

The pixel brightness of the raw image data represents the relative variation in attenuation across the sample within the image frame. The images are captured under sufficient X-ray intensity that the scintillator is in a transient state as its temperature increases during the exposure to the intense X-ray beam. The average pixel value was found to increase linearly with time, which is expected. If a scintillator is exposed to X-rays for too long the brightness of the fluorescence will decrease rapidly [6]. To account for this, a line was fit to each pixel value over time and the slope was subtracted to maintain only the constant term. This data was further processed to emphasize the contrast of the image data. Each image was filtered by treating each pixel independently as described in Eq. (1):

$$V = \text{abs}(v - m) \quad (1)$$

where,  $V$  is the filtered pixel value,  $v$  is the initial pixel value, and  $m$  is the mode of the first 50 frames for each pixel. The mode of the first 50 frames is assumed to be the initial background image of the sample as no laser polishing has occurred within these frames.

The filter emphasizes the contrast of the images, especially the keyhole, and can reveal the melt pool solidification front that is barely distinguishable in the raw video. The pixel of a filtered image represents the magnitude of the difference between a pixel and its initial value before laser polishing and thus is used to emphasize when the density is different from the initial value (i.e., molten or vapor state vs initial solid state). Filtered video and individual image frames can be found in the Appendix.

A composite image was produced by writing the maximum value over time for each pixel of the filtered video into a single image. This reveals the depth of the keyhole as the melt pool traverses the single feature in a single image. Saturated pixels can randomly appear in the video frames and these pixels would be emphasized by the act of recording a pixel's maximum value over time to produce said composite image. A 2D spatial median filter was applied to the composite image to eliminate the presence of any saturated pixels that randomly appear in the video as noise and would otherwise cause a speckle pattern in the composite image.

The keyhole boundary and its corresponding area and maximum depth were also measured for each video frame. The keyhole boundary was found using the Sobel operator in image processing software's (Mathworks, MATLAB 2022a) edge detection function and the keyhole geometry could be quantified as a function of time. The keyhole depth was determined by the distance between the surface and the deepest white pixel in a binarized image. The width was determined at a fixed distance just below the initial surface.

### 2.5. Post laser polishing sample analysis

Unpolished and laser polished surfaces were characterized using variable focus microscopy (Alicona, InfiniteFocus G4) to measure the top surface heights across the sample (Fig. 2). Cross sections of the Y–Z plane of the melt pool were performed by manually grinding the sample surface to remove material and polished with 1  $\mu\text{m}$  diamond solution to prepare for electroetching. An exposure of 7 s in 0.5 M HCl with a 5.7 V voltage bias was used for etching. The cathode was a platinum mesh and anode a titanium wire. At each step the melt pool Y–Z cross section was imaged after etching and the top melt width and melt depth were measured from the images revealing the overall melt pool shape in the Y–Z plane.

### 2.6. Ray tracing for energy input simulation

To describe the change of absorbing energy conditions in the keyhole, a 2D-ray tracing algorithm was used [7] assuming that each ray carries the integrated power of the circular beam of Gaussian shape through the related surface area, which is defined as the initial intensity. The rays are absorbed by the keyhole vapor in the keyhole and Fresnel absorption when striking a wall element. Classical optics was used to trace the rays within the keyholes, while the keyhole shapes were extracted from the X-ray images before, during, and after the surface feature.

## 3. Results

The high-speed X-ray imaging of the laser polishing process as the beam and melt pool transverse a single engineered feature reveals some interesting dynamics at play. As the melt pool approaches the feature it was observed that the keyhole begins to widen while decreasing in depth relative to the initial surface plane, thus a significant change in aspect ratio is observed. A change also occurs as the keyhole traverses down the opposite side of the surface feature except the keyhole narrows while gaining significant depth (Fig. 3). During these two events it appears that one of the walls of the keyhole slows or remains near stationary for a period of time.

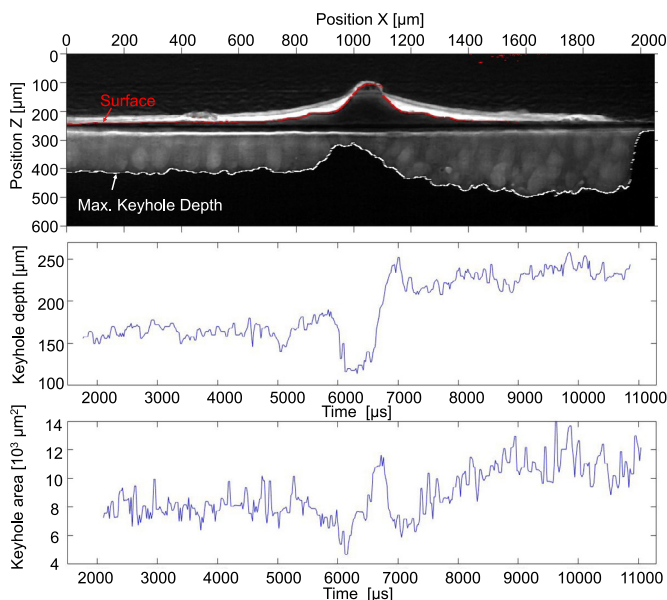


**Fig. 3.** The keyhole depth at each location shown through a composite image representing the maximum change in sample density over all video frames at the location of each pixel, as well as keyhole depth and keyhole area (X–Z plane) as a function of time.

When traversing up the surface feature the back wall of the keyhole moves slower than the front, leading to a widening of the keyhole in the X–Z plane (Fig. 4a). The opposite occurs while traversing down the feature as the front wall moves slower than the back wall. This causes the wide, shallow keyhole to again become narrow and

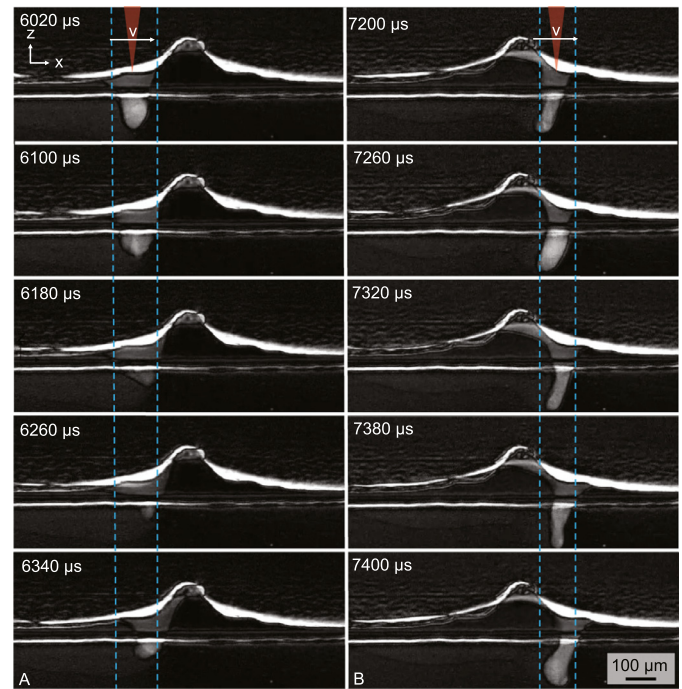


**Fig. 4.** Filtered images with 40  $\mu\text{s}$  spacing showing the stationary (or slow moving) rear keyhole wall as the melt ramps up and front keyhole wall as the melt ramps down the surface feature.

deep (Fig. 4b). The location of the keyhole's wall in the initial frames of each sequence, 6020  $\mu\text{s}$  and 7200  $\mu\text{s}$  are projected onto all corresponding frames with dashed blue lines in Fig. 4. The video is available in the Appendix.

As the keyhole begins to ramp up the feature, the front keyhole wall remains moving at near constant speed, while the back wall begins to slow. It is hypothesized that the slowing of the back keyhole wall is due to an increased in absorbed laser intensity from reflections off the surface feature and/or front lip of the keyhole. While descending the single feature, a similar affect is observed and can also be explained through an increase in reflection of the laser beam from the back wall into the front wall. The light reflected during this event from the back keyhole wall is incident to the front wall of which is not vertical and would result in continued reflections down into the keyhole, resulting in a narrower keyhole that is deeper than the initial, pre surface feature keyhole. It was observed that once this deeper keyhole was formed, it remained after the beam has moved beyond the feature and can be deemed as a new steady state with a deeper and narrower keyhole than the steady state before the melt pool traversed the surface feature.

Images of the polished cross-section confirmed the changed melt pool shape resulting from the keyhole shape variations and show the Y–Z plane width, which cannot be observed in the X-ray images as its orientation is into the page (Fig. 5). The cross sections revealed the same change in depth as observed in the X-rays and the change in width in the Y–Z plane was observed to have changed to a lesser degree.

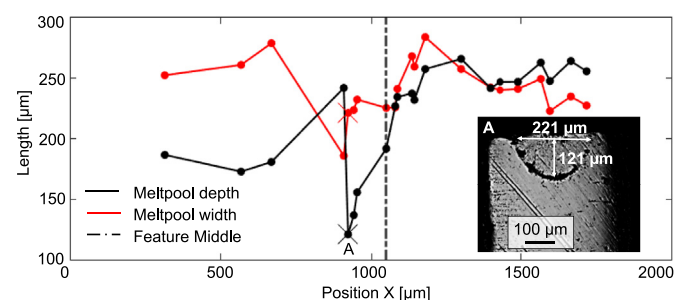


**Fig. 5.** Sample macrograph of cross-section and plot showing melt depth and width in Y–Z-plane.



The ray tracing simulation showed the shape of the keyhole can significantly alter the reflected rays' paths (Fig. 6). The keyhole shape before the feature shows a high total absorptance and supports many multiple reflections (Fig. 7). During the feature, the keyhole shape changes to less round keyhole openings, transferring more energy directly to the lower keyhole sections. After the surface feature, the keyhole is narrower, but the depth increased. The absorption versus depth calculated by ray tracing shows a significant increase in intensity absorbed for the bottom of the keyhole relative to the top.

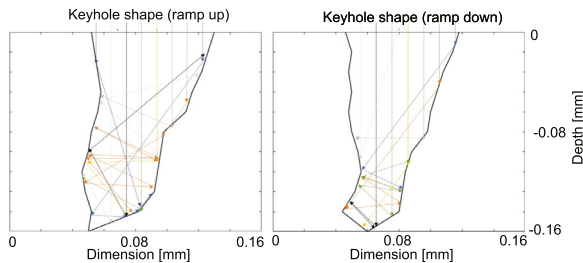


Fig. 6. Example ray tracing plots for the keyhole shape while the melt pool is ramping up and ramping down the surface feature.

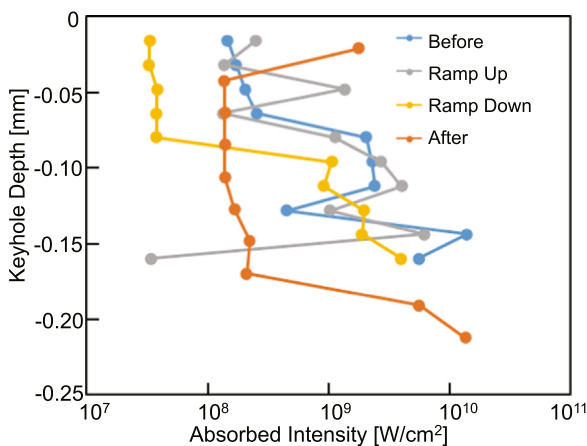


Fig. 7. Absorbed intensity within the keyhole as a function of keyhole depth for a keyhole shape before, ramping up, ramping down, and after the surface feature.

#### 4. Discussion

Based on careful observation and analysis of the high-speed X-ray imaging of the keyhole as it traverses the single surface feature, it is hypothesized that the laser beam is reflecting off the feature and melt pool surface, striking the wall of the keyhole furthest from the feature, and causing that wall to stay molten longer, hence appear to slow down relative to the other keyhole wall. As the laser beam approaches the feature, the reflections spread the energy of the beam over a larger area (elongate the melt pool in X-direction). At the same time, the keyhole width increases, leading to a wide keyhole opening and therefore to a reduced energy input in the higher keyhole sections and an overall more dispersed energy input due to multiple reflections. As the laser is moving down the downstream side of the feature, the laser beam is reflecting off the feature and back keyhole wall and shifts the front of the keyhole to a position ahead of where it would be if on a flat surface. This has the effect of preheating the region ahead of the laser beam and results in multiple reflections guiding the light deeper into the keyhole. The keyhole depth increases because of the increase in the energy density near the bottom of the keyhole (Fig. 7). Apparently, the keyhole top widening as the melt pool approaches the surface feature is the starting point of creating a new stable keyhole but now at different starting conditions compared to the evolution on a flat surface. The high intensity on the keyhole bottom seems to increase the keyhole depth, while the absorption in the upper keyhole part leads to conditions that the multiple reflections are mainly guided to the lower keyhole sections.

#### 5. Conclusion

Surface features influence more than the resulting surface quality of the process. When polishing in the keyhole regime, a significant influence on the keyhole and melt pool depth was found based on an initial surface feature. It was observed that induced variations of energy input into the keyhole caused by a surface feature can alter the keyhole shape. For the scale of this study, those changes remained after the surface feature when the laser was again moving over a flat surface. Experiments (or numerical simulations) of longer duration are needed to determine if the new keyhole shape is steady or slowly reverts to the geometry it had prior to traversing the surface feature. It was shown that surface features can alter the keyhole shape and can result in changed multiple reflection conditions, which can lead to a different keyhole shape after the feature at otherwise equal processing conditions. This implies that there is hysteresis present, and the melt pool/keyhole geometries are dependent not only on laser polishing parameters and current surface condition but also the surface condition that the melt pool has previously encountered. In practice, surface metrology or an in-situ monitoring device such as acoustic measurements of the keyhole characteristics may be necessary to determine when these drastic changes in keyhole shapes take place within a process field so that process parameters can be adjusted to maintain or rapidly revert back to the original melt pool conditions. Such an affect is relevant to a variety of fields, including but not limited to laser polishing, such as: metal additive manufacturing and micro-laser welding.

#### Declaration of Competing Interest

The authors declare the following financial interests/personal relationships which may be considered as potential competing interests:

#### Acknowledgments

This work was supported by National Science Foundation (NSF) grant [CMMI-1727366](#), the Deutsche Forschungsgemeinschaft project number [386371584](#) and Vetenskapsrådet (project number [2020-04250](#)). This research used resources of the Advanced Photon Source, a US Department of Energy (DOE) Office of Science user facility operated for the DOE Office of Science by Argonne National Laboratory under Contract No. [DE-AC02-06CH11357](#). The authors would like to thank Alex Deriy (APS) and Hemant Agiwal (UW-Madison) for their assistance in conducting the beamline experiments.

#### Appendix. Supplementary material

Detailed information on the experimental setup and original data files can be found in the Mendeley dataset [\[8\]](#).

#### References

- [1] Richter B, Blanke N, Werner C, Parab ND, Sun T, Vollertsen F, Pfefferkorn FE (2019) High-Speed X-ray Investigation of Melt Dynamics During Continuous-Wave Laser Remelting of Selective Laser Melted Co-Cr Alloy. *CIRP Annals* 68(1):229–232.
- [2] Kaplan A (1994) A Model of Deep Penetration Laser Welding Based on Calculation of the Keyhole Profile. *Journal of Physics D: Applied Physics* 27(9):1805.
- [3] Ki H, Mazumder J, Mohanty PS (2002) Modeling of Laser Keyhole Welding: Part II. Simulation of Keyhole Evolution, Velocity, Temperature Profile, and Experimental Verification. *Metallurgical and Materials Transactions A* 33(6):1831–1842.
- [4] Chongbunwatana K (2014) Simulation of Vapour Keyhole and Weld Pool Dynamics During Laser Beam Welding. *Production Engineering* 8(4):499–511.
- [5] Parab ND, Zhao C, Cunningham R, Escano LI, Fezzaa K, Everhart W, Rollett AD, Chen L, Sun T (2018) Ultrafast X-ray Imaging of Laser-Metal Additive Manufacturing Processes. *Journal of Synchrotron Radiation* 25:1467–1477.
- [6] Kastegren A (2019) Thermal Behaviour of Single-Crystal Scintillators for High-Speed X-ray Imaging. *Journal of Synchrotron Radiation* 26:205–214.
- [7] Volpp J, Vollertsen F (2016) Keyhole Stability During Laser Welding—Part I: Modeling and Evaluation. *Production Engineering* 10(4):443–457.
- [8] Pfefferkorn F, Radel T, Faue P, Klingbeil K, Richter B, Hassan M, Clarke SJ, Fezzaa K, Volpp J, Rathmann L, Moeller M (2023) High-Speed X-Ray Study of Process Dynamics Caused by Surface Features During Continuous-Wave Laser Polishing. *Mendeley Data* : V2. <https://doi.org/10.17632/4jgppjvbd2>.